



# Metal Substitution in Rutile TiO<sub>2</sub>: Segregation Energy and Conductivity

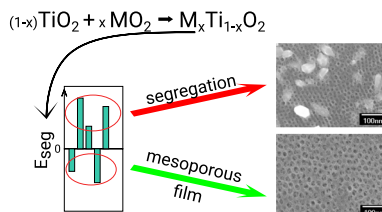
Katharina C. L. Bauerfeind<sup>1</sup> · Joachim Laun<sup>1</sup> · Marvin Frisch<sup>2</sup> · Ralph Kraehnert<sup>2</sup> · Thomas Bredow<sup>1</sup>

Received: 31 August 2021 / Accepted: 26 October 2021 / Published online: 23 November 2021  
© The Minerals, Metals & Materials Society 2021

## Abstract

State-of-the-art acidic oxygen evolution reaction catalysts are mainly based on mixed oxides of titanium and iridium or ruthenium. Because of its high chemical corrosion resistance and stability in acid, TiO<sub>2</sub> is a promising support material, yet with poor electrical conductivity. We herein theoretically examined the stability and the electronic properties of substituted rutile-phase titania, in which Ti is partly replaced by elements of the fourth, fifth and sixth period. For negative values of the calculated segregation energy, we conclude that the heteroelement M forms a solid solution for 25% or 50% substitution. For these heteroelements, we calculate the electrical conductivity. Since it is known that the electronic structure of transition metal oxides strongly depends on the applied theoretical method, we performed self-consistent optimizations of the Hartree-Fock contribution to the exchange functional in a hybrid functional for every compound. Experimentally, two favorable and two unfavorable elements were synthesized with 25% foreign metal concentration. The most promising candidates to improve the electronic properties of titania are Ta and Nb.

## Graphical Abstract



**Keywords** DFT · conductivity · doping · titania · OER · ab initio

## Introduction

Electrocatalytic systems play a pivotal role for matter and energy transfer with industrially relevant dimensions. With the aid of water electrolysis, sustainably produced electricity can be transferred into hydrogen and thus stored. Efficiency and costs of these systems depend crucially on the employed

catalysts which are typically based on noble metals ensuring stability and high catalytic activity.<sup>1</sup> Yet these metals are very costly and of limited global supply.<sup>2</sup>

Under acidic conditions, water splitting usually takes place in polymer electrolyte membrane (PEM) electrolyzer cells. In those, the limiting factor is not the hydrogen evolution reaction (HER), but the oxygen evolution reaction (OER). Common catalysts for the acidic OER are IrO<sub>2</sub> and RuO<sub>2</sub> as well as their mixed oxides with Ti.<sup>3–5</sup> The intrinsic catalytic properties are controlled by the composition and atomic distribution of the electrode material. Since the OER is a surface reaction, one step of reducing the noble metal content of the electrode is the limitation to the surface. The remainder of the electrode can consist of a conductive oxide of Ti combined with a less expensive and rare foreign metal in the rutile phase. A first step for new electrode design is finding

✉ Thomas Bredow  
bredow@thch.uni-bonn.de

Katharina C. L. Bauerfeind  
bauerfeind@thch.uni-bonn.de

<sup>1</sup> Mulliken Center for Theoretical Chemistry, Institute of Physical and Theoretical Chemistry, University of Bonn, Beringstr. 4-6, D-53115 Bonn, Germany

<sup>2</sup> Department of Chemistry, Technical University of Berlin, Straße des 17. Juni 124, D-10623 Berlin, Germany

a foreign metal that leads to a conducting material within the rutile matrix. Preliminary studies by Bernsmeier et al.<sup>6</sup> revealed that a minimum electrical conductivity was required to enable efficient charge transfer and promote catalytic OER activity. Un-doped, porous TiO<sub>2</sub> is not suitable as a support material, since its bulk conductivity lies below the conductivity threshold. Doping rutile with metallic or non-metallic heteroelements for more desirable properties has been studied under various aspects and is well documented in literature.<sup>7–11</sup> Among the plethora of literature on doped rutile, many theoretical studies investigating *d*- and *p*-block metal doping in order to increase the photocatalytic activity.<sup>12–25</sup>

The focus of the present study is on the formation of a solid solution of the heteroelement in the rutile matrix and the resulting electrical conductivity. Mixed oxides M<sub>x</sub>Ti<sub>1-x</sub>O<sub>2</sub> that are favorable in both aspects were recommended for synthesis and have been tested experimentally. From our previous combined experimental and theoretical study on Nb-doped TiO<sub>2</sub>, we are aware that the conductivity depends on the Nb concentration.<sup>26</sup> Here, we consider two fixed metal concentrations to focus on general trends with several theoretical methods. Therefore, we modeled the formation of a solid solution in the rutile phase by the following reaction:



with  $x = 0.5, 0.25$  and  $M = (\text{Sc}, \text{V}, \text{Cr}, \text{Mn}, \text{Fe}, \text{Co}, \text{Ni}, \text{Ga}, \text{Ge}, \text{Y}, \text{Zr}, \text{Nb}, \text{Mo}, \text{Ru}, \text{Rh}, \text{Pd}, \text{In}, \text{Sn}, \text{Sb}, \text{Te}, \text{Hf}, \text{Ta}, \text{W}, \text{Re}, \text{Os}, \text{Ir}, \text{Pt}, \text{Tl}, \text{Pb}, \text{Bi})$ . All oxides must have rutile structure. In the mixed compounds M<sub>0.5</sub>Ti<sub>0.5</sub>O<sub>2</sub> and M<sub>0.25</sub>Ti<sub>0.75</sub>O<sub>2</sub> the atoms of the heteroelement M are maximally separated. In this way we examine if the heteroelement has the tendency to segregate, i.e. to evenly distribute in the rutile matrix or to form a separate phase. We, therefore, denoted the calculated reaction energy corresponding to the above equation as *segregation energy*  $E_{\text{seg}}$ . A negative segregation energy indicates that the heteroelement M will form a solid solution.

In comparison with known mixed oxide systems,<sup>17,22,27</sup> the percentage of the foreign metal considered here is quite high, yet the conductivity at  $x = 0.5$  is a sufficient marker for further investigations, as known from our previous studies.<sup>26</sup> We are also aware that the chosen reaction and the corresponding segregation energy are an insufficient description of thermodynamic stability with respect to the M oxides in their equilibrium structures. This has been investigated theoretically before<sup>17,22,27</sup> and is not the scope of the present study. Stable oxides MO<sub>2</sub> with rutile structure do exist for 15 of the investigated metals, and others form distorted rutile structures.<sup>28,29</sup> Thus, not all of the MO<sub>2</sub> references are entirely artificial. Our simplified approach serves as a sufficient first step for further investigation or exclusion of possible dopants and aids in the development of superior

support materials for catalytically active species, e.g. electrocatalytic reactions. The theoretical results narrow down the number of laboratory experiments which must be performed. Experimental results for the most promising heteroelements are reported in the results section. In the next sections we describe the computational approach followed by a presentation of the computed segregation energies, experimental results and computed conductivities.

## Computational Details

Partial substitution of the Ti atoms by heteroelement M in the rutile lattice can lead to insulating, semiconducting or metallic ground states. In addition, substitution with transition metals can result in open-shell systems with strongly correlated *d*-electrons. It is well known that electronic properties such as the band gap or the electrical conductivity of such systems are often inaccurately described by standard Kohn-Sham density functional theory (DFT). Standard global hybrid functionals contain a fixed amount of Fock exchange in the exchange functional and are in general better suited for insulators and semiconductors than for metals. A more flexible approach is using the self-consistent dielectric-dependent hybrid (sc-DDH) functionals.<sup>30</sup> The percentage of Fock exchange is iteratively optimized for each system based on the inverse dielectric constant.<sup>31</sup>

In the present study we have applied a complementary theoretical approach combining a plane wave approach and a linear combination of atomic orbitals (LCAO) approach with CRYSTAL17. We compared the electronic end energetic properties obtained with generalized gradient approximation (GGA), *meta*-GGA and hybrid functionals, respectively. The computational details of both approaches are given below.

All plane wave DFT calculations were performed with the Vienna ab initio program (VASP) version 6.1.1<sup>32–34</sup> using the projector-augmented wave (PAW) approach of Joubert and Kresse.<sup>35, 36</sup> The respective POTCAR files containing the PAW parameters were taken from the VASP library. The PAWs with the largest valence-space available optimized for GW calculations, denoted as Ti\_sv\_GW, O\_GW and M\_sv\_GW, which include the semi-core *s* and *p* shells of the metals, were applied. Full structure relaxations were performed using a 900 eV energy cutoff for the plane wave basis sets. The Monkhorst Pack net was adjusted to the cell size. For the primitive unit cells (PUC) and the 1 × 1 × 2 supercells 4 × 4 × 6 and 4 × 4 × 3 grids were used, respectively. The GGA functional PBE<sup>37</sup> and the *meta*-GGA functional SCAN<sup>38</sup> were employed. Dispersion effects were taken into account by applying the D4 dispersion correction<sup>39–41</sup> (PBE-D4) and by the less-empirical van der Waals density functional SCAN + rVV10.<sup>42–44</sup> The threshold of the relaxation of

the electronic degrees of freedom (EDIFF) was set to  $10^{-6}$  eV with EDIFFG of -0.01 eV.

All LCAO calculations were performed with the crystalline orbital program CRYSTAL17 version 1.0.2.<sup>45,46</sup> The GGA functionals PBE<sup>37</sup> and PW91,<sup>47</sup> and the hybrid functional PW1PW,<sup>48,49</sup> which is based on PW91 including 20% Fock exchange, were used. In addition, the D3(BJ) correction by Grimme et al.<sup>50,51</sup> was applied in case of PBE and PW1PW. sc-DDH functionals were derived from PW1PW individually for all compounds and denoted as sc-PW1PW. All-electron Gaussian-type basis sets were used for O and Sc-Ge,<sup>52</sup> and ECP-based basis sets for Y-Te<sup>53</sup> and Hf-Po,<sup>54</sup> which are of consistent triple-zeta with polarization quality. A  $4 \times 4 \times 6$  Monkhorst-Pack and  $8 \times 8 \times 8$  Gilat net was used for geometry optimizations of the PUC, and a modified  $4 \times 4 \times 3$  Monkhorst-Pack net was used for all supercell calculations. The truncation criteria for bi-electronic integrals were set to  $10^{-7}$  for the overlap and penetration threshold for the Coulomb integrals, and for the overlap threshold for HF exchange integrals. For the pseudo overlap in the HF exchange series, the truncation criteria were set to  $10^{-14}$  and  $10^{-42}$  (TOLINTEG 7 7 7 14 42). The SCF accuracy was set to  $10^{-7}$  a.u. for geometry optimizations.

Most MO<sub>2</sub> and M<sub>0.5</sub>Ti<sub>0.5</sub>O<sub>2</sub> were calculated in their closed-shell states (denoted as non-magnetic (NM) in the following), in a ferromagnetic spin state (FM) and an antiferromagnetic spin state (AFM) with antiparallel spins at the substituted metals but an overall magnetic moment of zero. Elements without unpaired valence electrons such as M<sup>4+</sup> (Ge, Zr, Sn, Hf, Pb) were only calculated in the NM state. To achieve AFM spin ordering for M<sub>0.5</sub>Ti<sub>0.5</sub>O<sub>2</sub>,  $1 \times 1 \times 2$  supercells were necessary. The AFM supercells were created by substituting one metal atom in the PUC and then doubling the cell in the *c*-direction in order to ensure comparability with the NM and FM results. For FM compounds with possible high and low spin states, a high-spin initial configuration was defined and no further constraints were applied. Within VASP, FM spin states were achieved through spin-polarized calculations (ISPIN=2), defining an initial magnetization (MAGMOM). In AFM calculations, both options, total magnetic moment relaxation and fixation via NUPDOWN, were employed, while setting antiparallel initial spins on the substituted metal atoms. Within CRYSTAL, initial AFM spin states were achieved analogously by setting antiparallel spins (ATOMSPIN) and locking the total magnetic moment (SPINLOCK) to zero.

Resulting spin states with an energy difference of less than 2 kJ/mol per formula unit were considered energetically degenerate. If all three spin states were degenerate, the NM state was chosen. If FM and AFM spin states were degenerate and more stable than NM, FM was chosen. For FM results, the total spin density of the system is given.

For AFM results, the spin density per non-Ti metal atom is given.

For selected cases, the electronic structure in terms of an insulating or conducting ground state is of special interest. For global hybrid functionals, the band structure and the derived electrical conductivity strongly depend on the system-independent Fock exchange fraction. sc-DDH methods<sup>30</sup> have shown to provide more accurate absolute band positions and band gaps.<sup>55–57</sup> Therefore, the approach of Erba et al.<sup>31</sup> was used to determine the system-specific optimal Fock exchange for sc-PW1PW for rutile and selected mixed metal oxides. The resulting Fock exchange fractions are 15.1% (TiO<sub>2</sub>), 19.7% (Ge<sub>0.5</sub>Ti<sub>0.5</sub>O<sub>2</sub>), 58.6% (Sb<sub>0.5</sub>Ti<sub>0.5</sub>O<sub>2</sub>) and 12.7% (Pt<sub>0.5</sub>Ti<sub>0.5</sub>O<sub>2</sub>). For all other mixed metal oxides, the self-consistent procedure reduced the Fock exchange fraction to zero, corresponding to the PW91 GGA functional.

It was observed that the calculated absolute conductivities are very sensitive to the density of the applied *k*-point grid, in agreement with recommendations from the literature.<sup>58</sup> However, it was not possible to reach convergence due to increasing computational effort. Therefore, all electronic properties were calculated with sc-PW1PW, decreased integral thresholds (TOLINTEG 9 9 9 27 48), and denser  $24 \times 24 \times 24$  Monkhorst-Pack and  $48 \times 48 \times 48$  Gilat nets. For the calculated band structures, the *k*-vector path recommended by Curtarolo et al.<sup>59</sup> was applied to cover all special *k*-vector points. To estimate the electrical conductivity, the Boltzmann transport equation in relaxation time approximation as implemented as BOLTZTRA<sup>46</sup> in CRYSTAL17 was used. The conductivity  $\sigma$  was calculated at 298 K, with a relaxation time parameter  $\tau=1$  fs and finite-temperature schemes SMEAR of 0.01 a.u. By definition, the conductivity is calculated as a  $3 \times 3$  tensor for a three-dimensional system. Because of the tetragonal rutile structure, the *xx*- and *yy*-contributions are equal. Therefore, the small off-diagonal elements are discarded and the conductivity is estimated as the averaged diagonal elements  $\bar{\sigma}$  and separately as  $\sigma_{xx} = \sigma_{yy}$  and  $\sigma_{zz}$ .

## Results and Discussion

### Metal Dioxides in Rutile Structure

Before investigating mixed metal oxides, we give a short overview of rutile-type oxides with experimental references. Their calculated lattice parameters, band gaps, and magnetic ground states are given in the Supporting Information, Table SII. Lattice parameters of MO<sub>2</sub> with M = (Cr, Mn, Ge, Nb, Ru, Sn, Ir) are found in an overview of rutile structures by Bolzan.<sup>60</sup> V<sup>61</sup>, Mo<sup>62</sup>, Rh<sup>63</sup>, Re,<sup>64</sup> Os,<sup>65</sup> Pt<sup>66</sup> and Pb<sup>67</sup> also form rutile-type oxides. Rutile-type PdO<sub>2</sub> can be found in the Inorganic Crystal Structure Database, ICSD, with the index

647283.<sup>68</sup> The rutile structure is the most stable polymorph for  $M = (\text{Ge}, \text{Ru}, \text{Sn}, \text{Ir}, \text{Pb})$ .  $\text{IrO}_2$  and  $\text{RuO}_2$  are metallic oxides,<sup>69</sup>  $\text{PbO}_2$  is a small gap semiconductor and metallic when defective,<sup>70</sup>  $\text{GeO}_2$ <sup>71</sup> and  $\text{SnO}_2$ <sup>72</sup> are large gap semiconductors.  $\text{MnO}_2$  with rutile structure, pyrolusite, also occurs naturally,<sup>73</sup> while for  $M = (\text{V}, \text{Cr}, \text{Nb}, \text{Mo}, \text{Re}, \text{Os}, \text{Pt})$  the rutile polymorph is a meta-stable phase accessible at higher temperatures and/or pressures. In rutile structure  $\text{VO}_2$ ,  $\text{CrO}_2$ ,  $\text{NbO}_2$ , and  $\text{OsO}_2$  are metallic<sup>74</sup> and  $\text{MnO}_2$  is conducting at low temperatures.<sup>75</sup>

In our comparison of experimental and calculated lattice parameters, we omitted  $\text{PtO}_2$  and  $\text{PdO}_2$  due to incomplete experimental data as well as  $\text{NbO}_2$ ,  $\text{MoO}_2$  and  $\text{ReO}_2$ .  $\text{NbO}_2$  is only stable in rutile structure at 1300 K<sup>76</sup> and  $\text{MoO}_2$  occurs in rutile structure at 1533 K<sup>77</sup> which makes comparison with theoretical structure optimizations impossible. At ambient temperatures monoclinic or orthorhombic phases are preferred over rutile for  $\text{ReO}_2$ .<sup>78</sup>

For all remaining dioxides, we calculated the mean signed (MAD) and unsigned (MUD) percentile errors of the computed lattice parameters with respect to available experimental data, see Table 1. MAD and MUD are defined in Eqs. 1 and 2 in the Supplementary Information. All methods perform reasonably well with mean errors below 1%. With VASP, the maximum mean of the unsigned percent error is + 0.70% for the PBE functional. MAD is similar, 0.54%, indicating that PBE systematically overestimates the lattice parameters, in agreement with earlier benchmark tests.<sup>79</sup> Also, the small errors observed for SCAN, MUD = -0.18% and MAD = 0.35%, are in line with the observations by Tran et al. Surprisingly, PBE-D4 also overestimates the lattice parameters, while SCAN and SCAN+rVV10 slightly underestimate them.

Regarding CRYSTAL calculations, the hybrid functionals slightly underestimate and the GGAs overestimate the lattice parameters. Here, the largest unsigned error occurs for PW1PW-D3 with 0.79% and the largest signed error is found for PBE-D3 with + 0.47%, relatively close to the VASP results, indicating that the atomic basis sets are reasonable.

The maximum error for a single lattice parameter in VASP occurs for  $a(\text{RhO}_2)$  which is overestimated by 1.82–1.84%. In CRYSTAL, GGA calculations overestimate the  $c$  parameter of  $\text{GeO}_2$  by 1.82–2.02%. With hybrid functionals the  $c$  parameter of  $\text{VO}_2$  is underestimated by

-1.26/ - 1.38%. Generally, a slight underestimation of room temperature lattice parameters is reasonable, since calculations occur at 0 K.

In addition to the lattice parameters, the experimental band gaps are in general well reproduced. For  $\text{MnO}_2$ , hybrid methods erroneously predict a band gap; however, our approach simplifies its complicated magnetic structure.<sup>75</sup> With all other methods it is conducting. The other experimentally conducting oxides are uniformly predicted to have no band gaps.

## Mixed Metal Oxides

As mentioned in the introduction, we define the segregation energy  $E_{\text{seg}}$  per formula unit as

$$E_{\text{seg}} = E_{\text{M}_x\text{Ti}_{1-x}\text{O}_2} - xE_{\text{MO}_2} - (1-x)E_{\text{TiO}_2} \quad (1)$$

with  $x = (0.5, 0.25)$  as an indicator for possible formation of a solid solution. The energies refer to the total energies of the mixed metal oxide, the metal dioxide in rutile structure and pure  $\text{TiO}_2$  rutile with the respective functional. In order to take into account the approximations of our approach, we consider all  $M$  with a segregation energy of  $E_{\text{seg}} = \pm 4$  kJ/mol as possible candidates regardless of the sign. Only if the overall segregation energy is significantly larger than 4 kJ/mol do we assume segregation. Segregation energies smaller than - 4 kJ/mol indicate solubility according to our interpretation. Of course, this threshold is quite arbitrary, but the classification of  $M$  substituents does not change much with larger tolerances. Figure 1 shows  $E_{\text{seg}}$  for  $x = 0.5$  with all employed functionals. Results for  $x = 0.5, 0.25$  obtained with SCAN and PW1PW are shown in Fig. 2. Furthermore, all energies are given in Table SV in the supplementary Information.

For the majority of investigated metals, all methods provide similar trends. We averaged the differences of computed segregation energies,  $\overline{\Delta E}_{\text{seg}}$  (see Supporting Information Table SI), (i) for selected functionals with and without dispersion correction, and (ii) for the same functional (PBE) implemented in VASP and CRYSTAL. In this way, the effect of London dispersion and the basis set is investigated, respectively. Both differences are in most cases rather small, 0.3–1.3 kJ/mol, indicating that (i) London dispersion does

**Table 1** Mean signed (MAD) and unsigned (MUD), and maximum (MAX) percentile deviation for the lattice parameters of  $\text{MO}_2$

	VASP				CRYSTAL				
	SCAN	SCAN+rVV10	PBE	PBE-D4	PBE	PBE-D3	PW1PW	PW1PW-D3	PW91
MAD %	0.35	0.45	0.70	0.66	0.70	0.51	0.43	0.58	0.65
MUD %	-0.18	-0.34	0.54	0.39	0.47	0.16	-0.07	-0.25	0.41
MAX %	1.84 ( <i>a</i> Rh)	1.82 ( <i>a</i> Rh)	1.83 ( <i>a</i> Rh)	1.83 ( <i>a</i> Rh)	2.09 ( <i>c</i> Ge)	1.82 ( <i>c</i> Ge)	-1.26 ( <i>c</i> V)	-1.38 ( <i>c</i> V)	2.02 ( <i>c</i> Ge)

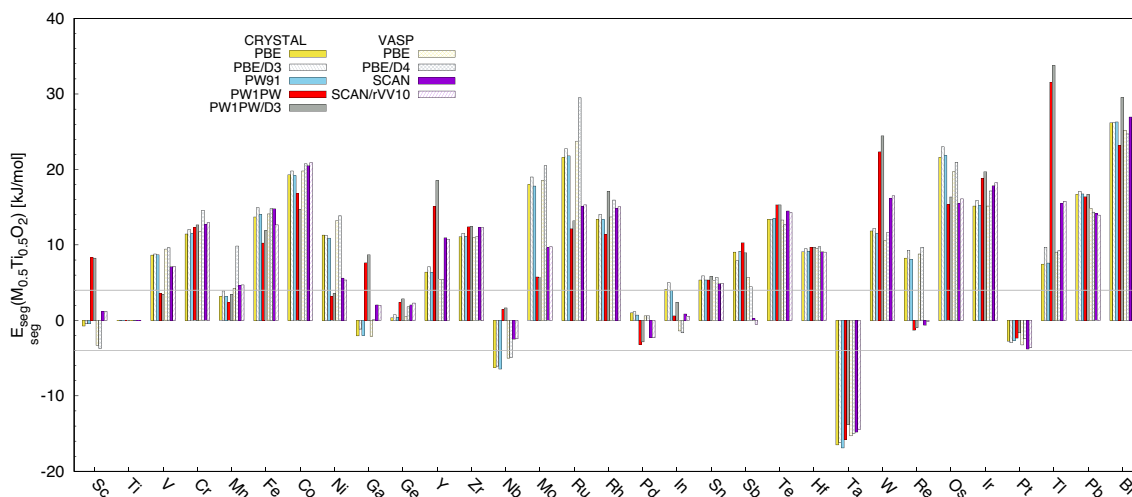


**Fig. 1** Segregation energies for  $M_{0.5}Ti_{0.5}O_2$  in rutile structure [kJ/mol] obtained with the selected functionals. Grey lines indicate the assumed  $\pm 4$  kJ/mol tolerance corridor.

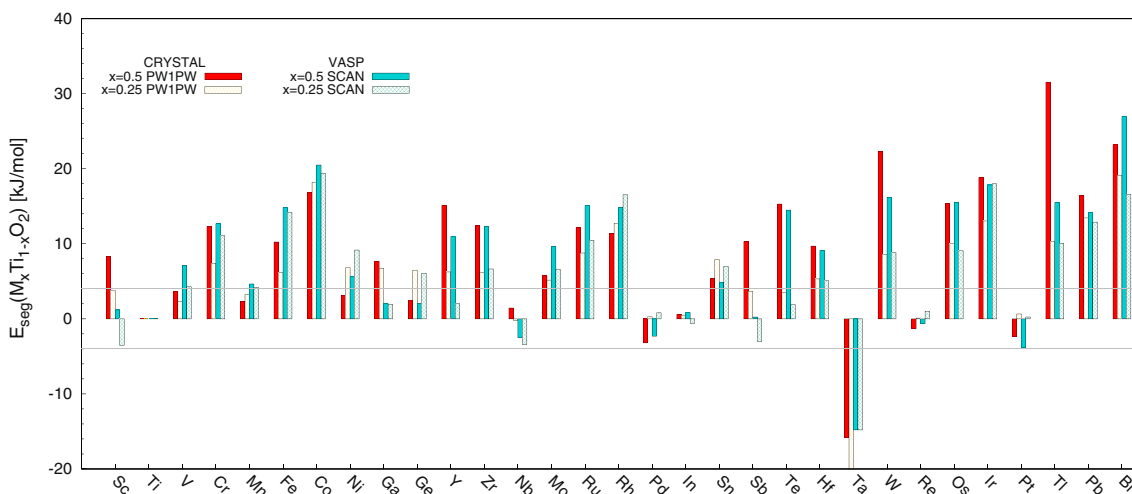


**Fig. 2** Segregation energies for  $M_{0.5}Ti_{0.5}O_2$  and  $M_{0.25}Ti_{0.75}O_2$  in rutile structure in kJ/mol with SCAN and PW1PW.

not play a significant role in Ti-M-O interaction, and (ii) the CRYSTAL pob-rev2 basis sets are reasonable. In CRYSTAL, the largest difference between segregation energies obtained with PBE and PBE-D3 is 2.2 kJ/mol for Tl and 6.4 kJ/mol for PW1PW and PW1PW-D3 for Bi. In VASP, the difference between PBE and PBE-D4 is more pronounced with a maximum of 5.8 kJ/mol for Ru. The difference is also pronounced for Cr, Mn, Ga, and Mo, equally resulting from differences in the minimum geometry and/or spin state. For Mn, the spin state is uniformly AFM and lattice parameters are similar; however, the PBE-D4 structure corresponds to a rather shallow minimum. Using the the same PBE minimum structures for both approaches, the energy difference between PBE and PBE-D4 segregation energies is reduced

to 0.5 kJ/mol. On the other hand, differences between SCAN and SCAN + rVV10 are very small with an average of 0.3 kJ/mol and a maximum of 2.3 kJ/mol.

The largest difference for PBE segregation energies calculated with VASP and CRYSTAL is 5.5 kJ/mol for In. It is, therefore, possible that the In pob-rev2 basis set is not optimal.

All methods predict positive segregation energies larger than 4 kJ/mol for  $M = Cr, Mn, Fe, Co, Y, Zr, Mo, Ru, Rh, Sn, Te, Hf, W, Os, Ir, Tl, Pb, \text{ and } Bi$ . For Ni and V, the use of hybrid methods lowers the segregation energy below 4 kJ/mol and also leads to the occurrence of band gaps. The same pattern applies for Mo at overall larger energies. Among the metals with positive segregation energies,



only Mo, Rh, W and Tl show method dependence of the magnetic ground state. Since their segregation energies are close to our predefined threshold, Mn and Ge will be considered candidates forming a solid solution. Pd, Pt and Ta are the only elements where all methods predict negative segregation energies. The segregation energy for Nb is positive with hybrid functionals (but below the threshold), while the GGA and meta-GGA functionals provide negative values for  $E_{\text{seg}}$ . For Sc, Ga, Pd, Sb, and Re, the methods give contradicting results for  $x = 0.5$ . In particular, for these systems we also investigated  $x = 0.25$ .

$M_{0.5}Ti_{0.5}O_2$  with  $M = \text{Sc, V, Ga, Y, In}$  and Tl are mostly predicted as FM systems with a delocalized total spin of 1.0 per primitive unit cell. With GGA, the well-known overdelocalization resulted in a closed shell ground state in some cases.  $M = \text{Co}$  and Ni oxides are also mostly predicted as being NM, while the other  $3d$  transition metals are either AFM or FM. Even with our simplified collinear approach, mixed oxides with  $M = \text{Mn}$  and Fe are most stable as AFM. Their heavier homologues,  $M = \text{Ru, Re,}$  and Os mixed oxides are also predicted as AFM. Mixed oxides with the other  $4d$  and  $5d$  transition metals are predicted as NM, except for Ta which is favored as FM. No trend can be found for  $M = \text{Mo}$  which ties in with our  $MO_2$  calculations.

The most stable spin state obtained for the respective  $M_{0.5}Ti_{0.5}O_2$  calculations was assumed for  $M_{0.25}Ti_{0.75}O_2$ . In order to retain the size of the  $1 \times 1 \times 2$  supercell, AFM spin states were approximated as FM, taking into account that the segregation energies might be less favorable with the smaller concentration.

As shown in Fig. 2, the positive segregation energies for  $M_{0.5}Ti_{0.5}O_2$  with  $M = \text{Cr, Mn, Fe, Co, Ni, Y, Zr, Mo, Ru, Rh, Sn, Te, Hf, W, Os, Ir, Tl, P, Bi, Po}$  are similar or even more positive with  $M_{0.25}Ti_{0.75}O_2$ . Increased Ti content confirms formerly ambiguous Ni and Mn as unsuitable candidates.

The segregation energies of  $M = \text{Ge, Pd, Pt}$  increase with decreasing M content, but are still within our threshold value. In contrast, Ta maintains a negative segregation energy and a solid solution with  $M = \text{Nb}$  becomes more favored. Re and In retain segregation energies close to zero independent of the concentration. Sc and Sb segregation energies become more negative with increasing Ti content, yet the sign remains functional dependent. It has to be noted that the particularly stable system  $Sc_{0.25}Ti_{0.75}O_2$  becomes NM during the optimization with SCAN. Both segregation energies for 25% Sb and Sc hint towards a possible solid solution.

Concluding from the segregation energies at 50% and 25% M concentration, we consider  $M = \text{Sc, Ga, Ge, Nb, Pd, In, Sb, Ta, Re,}$  and Pt as possible candidates for forming solid solutions with rutile  $TiO_2$ .

## Mesoporous $M_{0.25}Ti_{0.75}O_2$ Films

As a proof-of-concept of the theoretical results for the segregation energies, model-type mixed titania materials with  $x = 0.25$  and  $M = \text{Nb, Ta, Ir, Ru}$  were synthesized as representative examples using a previously established, well-controlled synthesis approach.<sup>6,26,80,81</sup> In brief, mesoporous films of the mixed oxides were prepared via dip-coating and evaporation-induced self-assembly (EISA).<sup>82</sup>

Titanium(IV) chloride ( $TiCl_4$ ) was chosen as the Ti-precursor and dissolved together with the corresponding metal precursor salt for  $M = \text{Nb, Ta, Ir, Ru}$  in a polar solvent (ethanol). By the ratio of the precursors, the composition of the resulting oxide material can be precisely adjusted. Our previous results indicate the production of various high surface area metal oxide films with adjustable layer thicknesses via dip-coating. Importantly, dip-coating can ensure a high degree of reproducibility for independent experiments due to its well-controlled atmosphere and parameters during deposition. The withdrawal rate controls the resulting layer thickness, for instance. By calcination at elevated temperatures in air, the as-deposited mesophase can be converted into a crystalline oxide phase upon a concomitant removal of the polymer template. In this study, calcination for 30 min at  $600^\circ\text{C}$  in air was chosen to afford crystalline oxide films with defined mesoporosity. Higher temperatures lead to pronounced crystallite growth and sintering effects, which are not desirable for the production of high surface area support materials for (electro-)catalytic applications.

As illustrated in Fig. 3, homogeneous films were obtained for Nb and Ta, whereas a pronounced crystallite growth and surface segregation effect can be observed for Ir and Ru. The distinct morphological differences provide clear evidence for the proposed segregation energies suggesting a partial segregation to take place for Ir and Ru during the calcination step at high temperature. This is in good agreement with observations from a previous study on mixed mesoporous titanium-iridium oxide films.<sup>4</sup>

For Nb and Ta, however, an incorporation into the titania lattice can be confirmed experimentally. No evidence for the formation of large crystallites or segregated domains at the pore wall surface of the oxide materials is given based on the obtained experimental results.

## Conductivity of Mixed Metal Oxides

For comparison with the literature, we first calculate the band structure, projected density of states (PDOS) and the electrical conductivity of rutile  $TiO_2$  without substitution (Fig. 4) with CRYSTAL17/sc-PW1PW/pob-TZVP-rev2.

The electronic properties of rutile  $TiO_2$  have been studied extensively in the literature at various theoretical levels.<sup>83–87</sup>

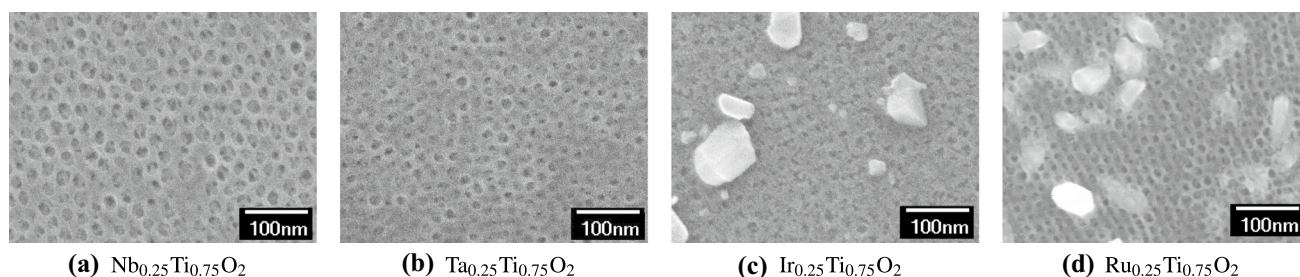


**Fig. 3** Top-view SEM images of different templated mesoporous  $M_{0.25}Ti_{0.75}O_2$ ,  $M = Nb$  in (a),  $Ta$  in (b),  $Ir$  in (c),  $Ru$  in (d), films synthesized via dip-coating in a controlled atmosphere and calcination for 30 min at 600°C in air. For  $M = Nb, Ta$ , homogeneous mesoporous films are obtained, indicating the formation of a solid

solution. For  $M = Ir, Ru$ , calcination at elevated temperature leads to a pronounced crystallite growth and partial segregation of  $MO_x$  species from the host titania lattice. The surface-segregated  $IrO_x$  and  $RuO_x$  crystals show a brighter contrast compared to the porous matrix, which strongly suggests Ir- or Ru-rich domains, respectively.

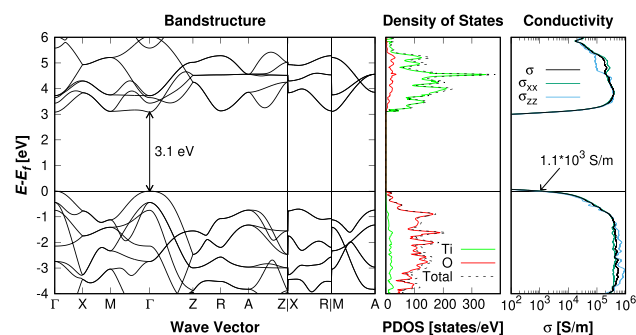


**Fig. 4** TiO<sub>2</sub>: Band structure, projected density of states (PDOS) in states/eV and electrical conductivity  $\sigma$  in S/m relative to the Fermi level at  $\epsilon_f = 0$  eV. The results are obtained with CRYSTAL17/sc-PW1PW/pob-TZVP-rev2.

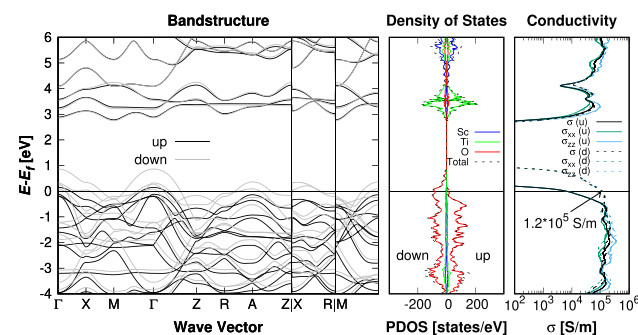


**Fig. 5**  $Sc_{0.5}Ti_{0.5}O_2$ : Band structure, projected density of states (PDOS) in states/eV and electrical conductivity  $\sigma$  in S/m relative to the Fermi level at  $\epsilon_f = 0$  eV.  $\alpha$  electron contributions are marked as ‘up’ and  $\beta$  contributions as ‘down’. The results are obtained with CRYSTAL17/sc-PW1PW/pob-TZVP-rev2.

Previous studies have shown that the application of hybrid functionals is necessary for the accurate electronic band gap prediction of semiconducting oxides.<sup>55,88–90</sup> In this work, the calculated fundamental band gap of 3.1 eV as obtained with CRYSTAL17/sc-PW1PW is in good agreement with experimental results of 3.3–3.6 eV.<sup>91,92</sup> Inspection of the PDOS shows that the top of the valence band is dominated by the O 2*p*-states while the bottom of the conduction band is mainly composed of Ti 3*d*-states, fully consistent with previous DFT studies.<sup>83,84</sup> As mentioned above (see “Computational Details” section), the absolute electrical conductivity is very sensitive to the applied *k*-point grid, depends on the relaxation time  $\tau$  and drastically changes in the energy range around the Fermi level. Therefore, its evaluation by comparison to experimental results is a critical challenge for theoretical approaches. Rutile TiO<sub>2</sub> conductivity at Fermi level is chosen as reference to study the substitution effect on electrical conductivity. The electrical conductivity of rutile TiO<sub>2</sub> is obtained as  $1.1 \times 10^3$  S/m at the Fermi level with CRYSTAL17/sc-PW1PW.

The formation of the mixed metal oxides leads to semiconductors in the case of  $Ge_{0.5}Ti_{0.5}O_2$  and  $Pt_{0.5}Ti_{0.5}O_2$ . The

band structures, PDOS and conductivities are given in Figure S1 in the SI, respectively. For  $Ge_{0.5}Ti_{0.5}O_2$ , sc-PW1PW calculations predict a direct fundamental band gap of 3.1 eV at the  $\Gamma$ -point. In comparison to TiO<sub>2</sub>, the resulting conductivity slightly decreases to  $0.7 \times 10^3$  S/m at the Fermi level. In the case of  $Pt_{0.5}Ti_{0.5}O_2$ , a significantly smaller fundamental band gap of 0.8 eV but only a slightly larger conductivity of  $0.8 \times 10^3$  S/m is calculated. Ge and Pt substitutions do not significantly increase the electrical conductivity in comparison to rutile TiO<sub>2</sub> and are, therefore, not considered promising catalyst support.

The mixed metal oxides  $Sc_{0.5}Ti_{0.5}O_2$ ,  $Ga_{0.5}Ti_{0.5}O_2$  and  $In_{0.5}Ti_{0.5}O_2$  form a group since the substitution of  $Ti^{4+}$  by  $M^{3+}$  (denoted as p-doping) leads to partial oxidation of the oxygen ions. The band structure, PDOS and conductivity of  $Sc_{0.5}Ti_{0.5}O_2$  are shown in Fig. 5. The corresponding graphs for  $Ga_{0.5}Ti_{0.5}O_2$  and  $In_{0.5}Ti_{0.5}O_2$  can be found in Figure S2 in the SI.

In all three cases, the top of the valence bands is dominated by the O 2*p*-states, in particular the  $\beta$  contributions.

The electrical conductivity increases compared to rutile  $\text{TiO}_2$  to  $1.2 \times 10^5 \text{ S/m}$  ( $\text{Sc}_{0.5}\text{Ti}_{0.5}\text{O}_2$ ),  $0.8 \times 10^5 \text{ S/m}$  ( $\text{Ga}_{0.5}\text{Ti}_{0.5}\text{O}_2$ ) and  $0.9 \times 10^5 \text{ S/m}$  ( $\text{In}_{0.5}\text{Ti}_{0.5}\text{O}_2$ ) at the Fermi level. For  $p$ -doped compounds, the majority of charge carriers are holes, which are introduced by  $\text{M}^{3+}$  impurities. To evaluate the electrical conductivity properly, the carrier mobility and concentration must be taken into account. Since the overall carrier concentration is constant for the given  $p$ -type compounds, the mobility might be the crucial property, which is not accessible by Boltzmann transport theory. In general, hole mobilities are lower compared to electron mobilities, which will be discussed later for the  $n$ -type doped compounds. Therefore, the given  $p$ -type mixed metal oxides might be a good starting point for photo- or electrochemical applications, which benefit from lower hole mobilities.

For  $\text{Pd}_{0.5}\text{Ti}_{0.5}\text{O}_2$ , the with *sc*-PW1PW calculated electrical conductivity of  $0.4 \times 10^5 \text{ S/m}$  at the Fermi level is increased in comparison to rutile  $\text{TiO}_2$ ; however, the number of states at this level is very low as can be seen in Fig. 6. For  $\text{Pd}_{0.25}\text{Ti}_{0.75}\text{O}_2$  a semiconducting state with a band gap of 0.3 eV is predicted. Standard PW1PW calculations for  $\text{Pd}_{0.5}\text{Ti}_{0.5}\text{O}_2$  and  $\text{Pd}_{0.25}\text{Ti}_{0.75}\text{O}_2$  (see Tables SII and SIII in the Supporting Information) result in indirect band gaps of 1.4 and 2.1 eV, respectively. Therefore, we do not consider  $\text{Pd}_{0.5}\text{Ti}_{0.5}\text{O}_2$  promising catalyst support.

For  $\text{Sb}_{0.5}\text{Ti}_{0.5}\text{O}_2$ , the calculated electrical conductivity at the Fermi level increases to  $1.9 \times 10^5 \text{ S/m}$ . The

corresponding band structure, PDOS and conductivity are given in Fig. 6. Substitution of Ti by Sb should give Sb in a formal  $\text{Sb}^{4+}$  oxidation state ( $4d^{10}5s^1$ ). However, calculations show that the  $5s$  state is very high in energy; therefore, the additional Sb electrons are preferentially transferred to  $\text{Ti}^{4+}$  cations which are reduced to  $\text{Ti}^{3+}$ , as seen by the intra-band states near the conduction band edge. This is confirmed by a population analysis of the states near the Fermi level. One must keep in mind that this solution suffers from the excessive delocalization of the  $\text{Ti}^{3+}$  states due to the application of the GGA-functional PW91 (*sc*-PW1PW). In addition, the overall number of states at the Fermi level is rather small and, therefore, we do not consider  $\text{Sb}_{0.5}\text{Ti}_{0.5}\text{O}_2$  promising catalyst support.

The mixed metal oxides  $\text{Nb}_{0.5}\text{Ti}_{0.5}\text{O}_2$ ,  $\text{Ta}_{0.5}\text{Ti}_{0.5}\text{O}_2$  and  $\text{Re}_{0.5}\text{Ti}_{0.5}\text{O}_2$  are classified as  $n$ -type doped oxides. For  $\text{Re}_{0.5}\text{Ti}_{0.5}\text{O}_2$ , the band structure, PDOS and corresponding conductivity are given in Fig. 7 (bottom). Inspection of the PDOS shows that the states at the Fermi level are dominated by Re  $d$ -orbitals. The electrical conductivity calculated with CRYSTAL17/*sc*-PW1PW/*pob*-TZVP-*rev2* is  $3.5 \times 10^5 \text{ S/m}$ . Since this is the highest calculated conductivity of all considered compounds,  $\text{Re}_{0.5}\text{Ti}_{0.5}\text{O}_2$  is in principle a promising mixed metal oxide for conductive catalyst supports. However, the occurrence of the unstable weakly radioactive isotope  $^{187}\text{Re}$  in combination with the limited supply and the resulting high price, we do not recommend the synthesis of  $\text{Re}_{0.5}\text{Ti}_{0.5}\text{O}_2$  in the first place.

On DFT level, Nb- and Ta-doped rutile  $\text{TiO}_2$  have been studied extensively in the literature.<sup>89,90,93,94</sup> In these studies, a semiconducting character is predicted for low dopant concentrations up to 6%. In the present study, the mixed metal oxides  $\text{Nb}_{0.5}\text{Ti}_{0.5}\text{O}_2$  and  $\text{Ta}_{0.5}\text{Ti}_{0.5}\text{O}_2$  show metallic behavior as can be seen by the calculated band structures and PDOS in Fig. 7. The corresponding electrical conductivities at the Fermi level are calculated as  $2.6 \times 10^5 \text{ S/m}$  ( $\text{Nb}_{0.5}\text{Ti}_{0.5}\text{O}_2$ ) and  $2.9 \times 10^5 \text{ S/m}$  ( $\text{Ta}_{0.5}\text{Ti}_{0.5}\text{O}_2$ ). In both cases, inspection of the PDOS show that the states at the Fermi level are dominated by Ti  $3d$ -, Nb  $4d$ - and Ta  $5d$ -orbitals, which is in accordance with recent DFT-studies.<sup>26,90,93</sup> The combination of favorable segregation energy and highly increased electrical conductivity leads to the recommendation of  $\text{Nb}_{0.5}\text{Ti}_{0.5}\text{O}_2$  and  $\text{Ta}_{0.5}\text{Ti}_{0.5}\text{O}_2$  for synthesis of support materials.

## Summary

We investigated the segregation energies of rutile  $\text{M}_x\text{Ti}_{1-x}\text{O}_2$  with  $x = 0.25, 0.5$  and  $\text{M} = (\text{Sc}, \text{V}, \text{Cr}, \text{Mn}, \text{Fe}, \text{Co}, \text{Ni}, \text{Ga}, \text{Ge}, \text{Y}, \text{Zr}, \text{Nb}, \text{Mo}, \text{Ru}, \text{Rh}, \text{Pd}, \text{In}, \text{Sn}, \text{Sb}, \text{Te}, \text{Hf}, \text{Ta}, \text{W}, \text{Re}, \text{Os}, \text{Ir}, \text{Pt}, \text{Tl}, \text{Pb}, \text{Bi})$  with GGA, *meta*-GGA, hybrid functionals, and dispersion corrections. All methods yield accurate lattice parameters and, within their expected errors,

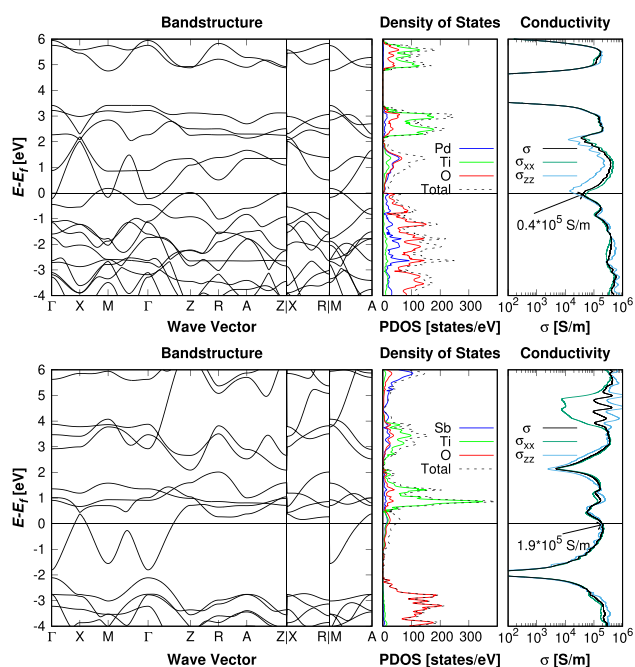


**Fig. 6**  $\text{Pd}_{0.5}\text{Ti}_{0.5}\text{O}_2$ (top) and  $\text{Sb}_{0.5}\text{Ti}_{0.5}\text{O}_2$ (bottom): Band structure, projected density of states (PDOS) in states/eV and electrical conductivity  $\sigma$  in S/m relative to the Fermi level at  $e_f = 0 \text{ eV}$ . The results are obtained with CRYSTAL17/*sc*-PW1PW/*pob*-TZVP-*rev2*.



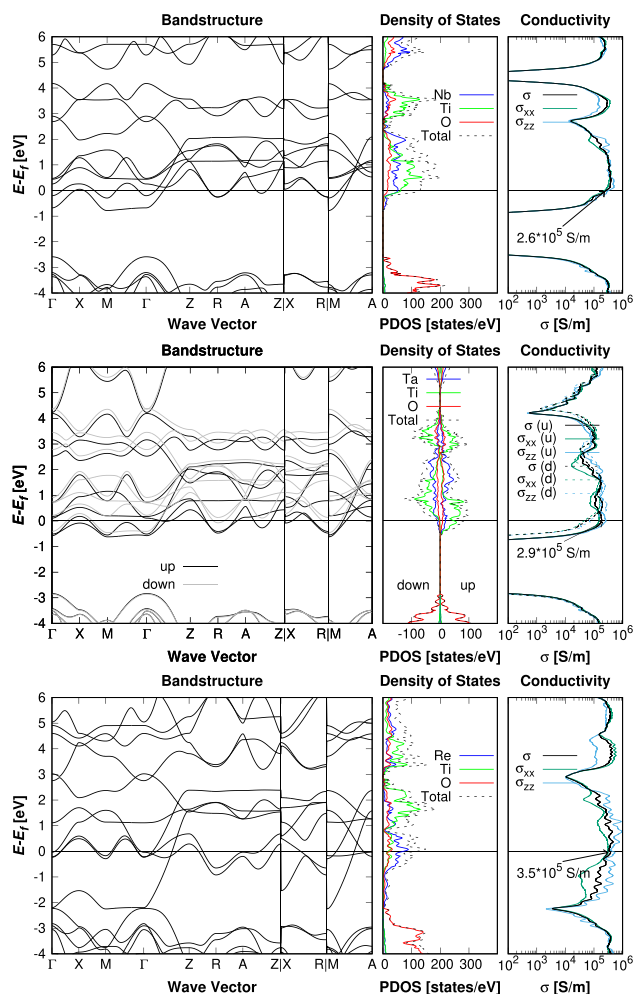


**Fig. 7** Nb<sub>0.5</sub>Ti<sub>0.5</sub>O<sub>2</sub>(top), Ta<sub>0.5</sub>Ti<sub>0.5</sub>O<sub>2</sub>(middle) and Re<sub>0.5</sub>Ti<sub>0.5</sub>O<sub>2</sub>(bottom): Band structure, projected density of states (PDOS) in states/eV and conductivity  $\sigma$  in S/m relative to the Fermi level at  $\epsilon_f = 0$  eV.  $\alpha$  electron contributions are marked as ‘up’ and  $\beta$  contributions as ‘down’. The results are obtained with CRYSTAL17/sc-PW1PW/pob-TZVP-rev2.

band gaps of the experimental rutile MO<sub>2</sub> structures. For the majority of metals we find the same trends for the magnetic ground state and also for a positive segregation energy with all methods. Segregation energies for M<sub>x</sub>Ti<sub>1-x</sub>O<sub>2</sub> with  $x = 0.25$  were calculated with *meta*-GGA SCAN and the hybrid functional PW1PW. For this smaller fraction M = Sc, Ga, Ge, Nb, Pd, In, Sb, Ta, Re, and Pt have segregation energies that may allow formation of solid solutions. For Nb, Ta, Ru and Ir mesoporous M<sub>0.25</sub>Ti<sub>0.75</sub>O<sub>2</sub> films were prepared via dip-coating. As hinted by the segregation energies, Ru and Ir exhibit crystallite growth and segregation at the surface, whereas Nb and Ta are incorporated into the titania lattice. Investigation of the band structures and conductivities of M<sub>0.5</sub>Ti<sub>0.5</sub>O<sub>2</sub> with M= Sc, Ga, Ge, Nb, Pd, In, Sb, Ta, Re, and Pt with sc-PW1PW confirm Nb and Ta as promising candidates for synthesis of support materials.

**Supplementary Information** The online version contains supplementary material available at <https://doi.org/10.1007/s11664-021-09318-4>.

**Acknowledgments** The authors gratefully acknowledge financial support by BMBF (Bundesministerium für Bildung und Forschung) ATOKAT: *Atomar dünn beschichtete poröse Elektroden als neuartige Katalysatoren für die Wasser-Elektrolyse*(03EK3052C). KB and JL thank the University of Bonn for providing computer time on the Bonna cluster.

**Author Contributions** KB and JL contributed equally to this work. KB contributed to all plane wave calculations, JL contributed to all LCAO calculations. MF contributed to all experimental aspects. KB, JL & MF contributed to the writing and editing of the manuscript. TB & RK conceived the study, contributed to the writing and editing of the manuscript.

**Conflict of interest** The authors declare that they have no conflict of interest.

## References

1. T. Reier, M. Oezaslan, P. Strasser, Electrocatalytic oxygen evolution reaction (OER) on Ru, Ir, and Pt catalysts: a comparative study of nanoparticles and bulk materials. *ACS Catal.* 2(8), 1765 (2012). <https://doi.org/10.1021/cs3003098>
2. U.S. Geological Survey. Mineral commodity summaries 2021: U.S. geological survey (2021). <https://doi.org/10.3133/mcs2021>
3. M. Yagi, E. Tomita, S. Sakita, T. Kuwabara, K. Nagai, Self-assembly of active IrO<sub>2</sub> colloid catalyst on an ITO electrode for efficient electrochemical water oxidation. *J. Phys. Chem. B* 109(46), 21489 (2005). <https://doi.org/10.1021/jp0550208>
4. M. Bernicke, D. Bernsmeier, B. Paul, R. Schmack, A. Bergmann, P. Strasser, E. Ortel, R. Kraehnert, Tailored mesoporous Ir/TiO<sub>x</sub>: Identification of structure-activity relationships for an efficient oxygen evolution reaction. *J. Catal.* 376, 209 (2019). <https://doi.org/10.1016/j.jcat.2019.06.044>
5. E. Oakton, D. Lebedev, M. Povia, D.F. Abbott, E. Fabbri, A. Fedorov, M. Nachtegaal, C. Copéret, T.J. Schmidt, IrO<sub>2</sub>-TiO<sub>2</sub>: a high-surface-area, active, and stable electrocatalyst for the oxygen evolution reaction. *ACS Catal.* 7(4), 2346 (2017). <https://doi.org/10.1021/acscatal.6b03246>
6. D. Bernsmeier, M. Bernicke, R. Schmack, R. Sachse, B. Paul, A. Bergmann, P. Strasser, E. Ortel, R. Kraehnert, Oxygen evolution catalysts based on Ir-Ti mixed oxides with templated mesopore structure: impact of ir on activity and conductivity. *ChemSuschem* 11(14), 2367 (2018). <https://doi.org/10.1002/cssc.201800932>
7. F. Huang, A. Yan, H. Zhao, in *Semiconductor Photocatalysis: Materials, Mechanisms and Applications* (IntechOpen, 2016), p. 31. <https://doi.org/10.5772/63234>
8. T.L. Thompson, J.T. Yates, Surface science studies of the photoactivation of TiO<sub>2</sub> new photochemical processes. *Chem. Rev.* 106(10), 4428 (2006). <https://doi.org/10.1021/cr050172k>
9. R. Dagherir, P. Drogui, D. Robert, Modified TiO<sub>2</sub> for environmental photocatalytic applications: a review. *Ind. Eng. Chem. Res.* 52(10), 3581 (2013). <https://doi.org/10.1021/ie303468t>
10. M. Kapilashrami, Y. Zhang, Y.S. Liu, A. Hagfeldt, J. Guo, Probing the optical property and electronic structure of TiO<sub>2</sub> nanomaterials for renewable energy applications. *Chem. Rev.* 114(19), 9662 (2014). <https://doi.org/10.1021/cr5000893>
11. J. Schneider, M. Matsuoka, M. Takeuchi, J. Zhang, Y. Horiuchi, M. Anpo, D.W. Bahnemann, Understanding TiO<sub>2</sub> photocatalysis:

- mechanisms and materials. *Chem. Rev.* 114(19), 9919 (2014). <https://doi.org/10.1021/cr5001892>
12. T. Umehayashi, T. Yamaki, H. Itoh, K. Asai, Analysis of electronic structures of 3d transition metal-doped TiO<sub>2</sub> based on band calculations. *J. Phys. Chem. Solids* 63(10), 1909 (2002). [https://doi.org/10.1016/S0022-3697\(02\)00177-4](https://doi.org/10.1016/S0022-3697(02)00177-4)
  13. G. Shao, Electronic structures of manganese-doped rutile TiO<sub>2</sub> from first principles. *J. Phys. Chem. C* 112(47), 18677 (2008). <https://doi.org/10.1021/jp8043797>
  14. L.K. Zhang, B. Wu, M. Wang, L. Chen, G.X. Ye, T. Chen, H.L. Liu, C.R. Huang, J.L. Li, *Adv. Mat. Res.* (2012). <https://doi.org/10.4028/www.scientific.net/AMR.399-401.1789>
  15. A. Stashans, J. Escobar, Effects of vanadium impurity on TiO<sub>2</sub> properties. *Int. J. Mod. Phys. B* 29(15), 1550094 (2015). <https://doi.org/10.1142/S0217979215500940>
  16. M. Saini, M. Kumar, T. Som, ab initio study of 3d transition metal-doping effects in rutile-TiO<sub>2</sub>: role of bandgap tunability in conductivity behaviour. *Appl. Surf. Sci.* 418, 302 (2017). <https://doi.org/10.1016/j.apsusc.2017.01.262>
  17. D. Xia, Q. Hou, Y. Guan, Z. Xu, M. Chen, First-principle study on the magnetic and optical properties of TiO<sub>2</sub> doped with different valence Fe. *Chem. Phys.* 539, 110949 (2020). <https://doi.org/10.1016/j.chemphys.2020.110949>
  18. A. Iwaszuk, M. Nolan, Electronic structure and reactivity of Ce- and Zr-doped TiO<sub>2</sub>: assessing the reliability of density functional theory approaches. *J. Phys. Chem. C* 115(26), 12995 (2011). <https://doi.org/10.1021/jp203112p>
  19. K.K. Ghuman, C.V. Singh, A DFT+ U study of (Rh, Nb)-codoped rutile TiO<sub>2</sub>. *J. Phys. Condens. Matter* 25(8), 085501 (2013). <https://doi.org/10.1088/0953-8984/25/8/085501>
  20. K. Song, X. Han, G. Shao, Electronic properties of rutile TiO<sub>2</sub> doped with 4d transition metals: first-principles study. *J. Alloys Compd.* 551, 118 (2013). <https://doi.org/10.1016/j.jallcom.2012.09.077>
  21. X. Lu, T. Zhao, X. Gao, J. Ren, X. Yan, P. La, Investigation of Mo-, Pt-, and Rh-doped rutile TiO<sub>2</sub> based on first-principles calculations. *AIP Adv.* 8(7), 075014 (2018). <https://doi.org/10.1063/1.5038776>
  22. J. Belošević-Čavor, V. Koteski, A. Umičević, V. Ivanovski, Effect of 5d transition metals doping on the photocatalytic properties of rutile TiO<sub>2</sub>. *Comput. Mater. Sci.* 151, 328 (2018). <https://doi.org/10.1016/j.commatsci.2018.05.022>
  23. P.K. Jha, S.K. Gupta, I. Lukačević, Electronic structure, photocatalytic properties and phonon dispersions of X-doped (X= N, B and Pt) rutile TiO<sub>2</sub> from density functional theory. *Solid State Sci.* 22, 8 (2013). <https://doi.org/10.1016/j.solidstatesciences.2013.05.003>
  24. A. Iwaszuk, M. Nolan, Charge compensation in trivalent cation doped bulk rutile TiO<sub>2</sub>. *J. Phys. Cond. Mat.* 23(33), 334207 (2011). <https://doi.org/10.1088/0953-8984/23/33/334207>
  25. M.O. Atambo, D. Varsano, A. Ferretti, S.S. Ataei, M.J. Caldas, E. Molinari, A. Selloni, Electronic and optical properties of doped TiO<sub>2</sub> by many-body perturbation theory. *Phys. Rev. Mater.* 3, 045401 (2019). <https://doi.org/10.1103/PhysRevMaterials.3.045401>
  26. M. Frisch, J. Laun, J. Marquardt, A. Arinchtin, K. Bauerfeind, D. Bernsmeier, M. Bernicke, T. Bredow, R. Kraehnert, Bridging experiment and theory: enhancing the electrical conductivities of soft-templated niobium-doped mesoporous titania films. *Phys. Chem. Chem. Phys.* 23, 3219 (2021). <https://doi.org/10.1039/D0CP06544G>
  27. J. Dai, L. Wang, X. Wu, Y. Song, R. Yang, Effects of alloying elements on the stability of TiO<sub>2</sub> and their diffusion properties studied by first principles calculations. *Mater. Today Commun.* 17, 40 (2018). <https://doi.org/10.1016/j.mtcomm.2018.08.007>
  28. W.H. Baur, The rutile type and its derivatives. *Crystallogr. Rev.* 13(1), 65 (2007). <https://doi.org/10.1080/08893110701433435>
  29. D. Romanov, V. Skrobot, Distortions of octahedra in rutile-type structures of transition element dioxides. *Glass Phys. Chem.* 35(5), 518 (2009). <https://doi.org/10.1134/S1087659609050101>
  30. J.H. Skone, M. Govoni, G. Galli, Self-consistent hybrid functional for condensed systems. *Phys. Rev. B* 89(19), 195112 (2014). <https://doi.org/10.1103/PhysRevB.89.195112>
  31. A. Erba, Self-consistent hybrid functionals for solids: a fully-automated implementation. *J. Condens. Mat. Phys.* (2017). <https://doi.org/10.1088/1361-648X/aa7823>
  32. G. Kresse, J. Furthmüller, Efficient iterative schemes for ab initio total-energy calculations using a plane-wave basis set. *Phys. Rev. B* 54(16), 11169 (1996). <https://doi.org/10.1103/PhysRevB.54.11169>
  33. G. Kresse, J. Furthmüller, Efficiency of ab-initio total energy calculations for metals and semiconductors using a plane-wave basis set. *Comput. Mater. Sci.* 6(1), 15 (1996). [https://doi.org/10.1016/0927-0256\(96\)00008-0](https://doi.org/10.1016/0927-0256(96)00008-0)
  34. G. Kresse, J. Hafner, Ab initio molecular dynamics for liquid metals. *Phys. Rev. B* 47(1), 558 (1993). <https://doi.org/10.1103/PhysRevB.47.558>
  35. P.E. Blöchl, Projector augmented-wave method. *Phys. Rev. B* 50(24), 17953 (1994). <https://doi.org/10.1103/PhysRevB.50.17953>
  36. G. Kresse, D. Joubert, From ultrasoft pseudopotentials to the projector augmented-wave method. *Phys. Rev. B* 59(3), 1758 (1999). <https://doi.org/10.1103/PhysRevB.59.1758>
  37. J.P. Perdew, K. Burke, M. Ernzerhof, Generalized gradient approximation made simple. *Phys. Rev. Lett.* 77(18), 3865 (1996). <https://doi.org/10.1103/PhysRevLett.77.3865>
  38. J. Sun, A. Ruzsinszky, J.P. Perdew, Strongly constrained and appropriately normed semilocal density functional. *Phys. Rev. Lett.* 115(3), 036402 (2015). <https://doi.org/10.1103/PhysRevLett.115.036402>
  39. E. Caldeweyher, C. Bannwarth, S. Grimme, Extension of the d3 dispersion coefficient model. *J. Chem. Phys.* (2017). <https://doi.org/10.1063/1.4993215>
  40. E. Caldeweyher, S. Ehlert, A. Hansen, H. Neugebauer, S. Spicher, C. Bannwarth, S. Grimme, A generally applicable atomic-charge dependent london dispersion correction. *J. Chem. Phys.* 150(15), 154122 (2019). <https://doi.org/10.1063/1.5090222>
  41. E. Caldeweyher, J.M. Mewes, S. Ehlert, S. Grimme, Extension and evaluation of the d4 london-dispersion model for periodic systems. *Phys. Chem. Chem. Phys.* 22(16), 8499 (2020). <https://doi.org/10.1039/D0CP00502A>
  42. J. Klimeš, D.R. Bowler, A. Michaelides, Chemical accuracy for the van der waals density functional. *J. Phys. Cond. Mat.* 22(2), 022201 (2009). <https://doi.org/10.1088/0953-8984/22/2/022201>
  43. J. Klimeš, D.R. Bowler, A. Michaelides, Van der waals density functionals applied to solids. *Phys. Rev. B* 83(19), 195131 (2011). <https://doi.org/10.1103/PhysRevB.83.195131>
  44. H. Peng, Z.H. Yang, J.P. Perdew, J. Sun, Versatile van der waals density functional based on a meta-generalized gradient approximation. *Phys. Rev. X* 6(4), 041005 (2016). <https://doi.org/10.1103/PhysRevX.6.041005>
  45. R. Dovesi, A. Erba, R. Orlando, C.M. Zicovich-Wilson, B. Civalleri, L. Maschio, M. Rérat, S. Casassa, J. Baima, S. Salustro et al., Quantum-mechanical condensed matter simulations with crystal. *WIREs Comput. Mol. Sci.* 8, 1360 (2018). <https://doi.org/10.1002/wcms.1360>
  46. R. Dovesi, V. Saunders, C. Roetti, R. Orlando, C. Zicovich-Wilson, F. Pascale, B. Civalleri, K. Doll, N. Harrison, I. Bush, I. D'Arco, M. Llunell, M. Causa, Y. Noel, A. Erba, M. Rerat, C.S. Crystal17 user's manual. University of Torino, Torino (2017)

47. J.P. Perdew, Y. Wang, Accurate and simple analytic representation of the electron-gas correlation energy. *Phys. Rev. B* 45(23), 13244 (1992). <https://doi.org/10.1103/PhysRevB.45.13244>
48. C. Adamo, V. Barone, Exchange functionals with improved long-range behavior and adiabatic connection methods without adjustable parameters: The m PW and m PW1PW models. *J. Chem. Phys.* 108(2), 664 (1998). <https://doi.org/10.1063/1.475428>
49. T. Bredow, A.R. Gerson, Effect of exchange and correlation on bulk properties of MgO, NiO, and CoO. *Phys. Rev. B* 61(8), 5194 (2000). <https://doi.org/10.1103/PhysRevB.61.5194>
50. S. Grimme, J. Antony, S. Ehrlich, H. Krieg, A consistent and accurate ab initio parametrization of density functional dispersion correction (dft-d) for the 94 elements H-Pu. *J. Chem. Phys.* 132(15), 154104 (2010). <https://doi.org/10.1063/1.3382344>
51. S. Grimme, S. Ehrlich, L. Goerigk, Effect of the damping function in dispersion corrected density functional theory. *J. Comput. Chem.* 32(7), 1456 (2011). <https://doi.org/10.1002/jcc.21759>
52. D.V. Oliveira, J. Laun, M.F. Peintinger, T. Bredow, Bsse-correction scheme for consistent gaussian basis sets of double-and triple-zeta valence with polarization quality for solid-state calculations. *J. Comput. Chem.* 40, 2364 (2019). <https://doi.org/10.1002/jcc.26013>
53. J. Laun, D. Vilela Oliveira, T. Bredow, Consistent gaussian basis sets of double-and triple-zeta valence with polarization quality of the fifth period for solid-state calculations. *J. Computat. Chem.* 39(19), 1285 (2018). <https://doi.org/10.1002/jcc.25195>
54. J. Laun, T. Bredow, Bsse-corrected consistent gaussian basis sets of triple-zeta valence with polarization quality of the sixth period for solid-state calculations. *J. Comput. Chem.* 42(15), 1064 (2021). <https://doi.org/10.1002/jcc.26521>
55. J. He, C. Franchini, Assessing the performance of self-consistent hybrid functional for band gap calculation in oxide semiconductors. *J. Phys. Condens. Mat.* (2017). <https://doi.org/10.1088/1361-648X/aa867e>
56. D. Fritsch, B.J. Morgan, A. Walsh, Self-consistent hybrid functional calculations: implications for structural, electronic, and optical properties of oxide semiconductors. *Nanoscale Res. Lett.* 12(1), 1 (2017). <https://doi.org/10.1186/s11671-016-1779-9>
57. Y. Hinuma, Y. Kumagai, I. Tanaka, F. Oba, Band alignment of semiconductors and insulators using dielectric-dependent hybrid functionals: toward high-throughput evaluation. *Phys. Rev. B* 95(7), 075302 (2017). <https://doi.org/10.1103/PhysRevB.95.075302>
58. G.K.H. Madsen, J. Carrete, M.J. Verstraete, BoltzTraP2, a program for interpolating band structures and calculating semi-classical transport coefficients. *Comput. Phys. Commun.* 231, 140 (2018). <https://doi.org/10.1016/j.cpc.2018.05.010>
59. W. Setyawan, S. Curtarolo, High-throughput electronic band structure calculations: challenges and tools. *Comput. Mater. Sci.* 49(2), 299 (2010). <https://doi.org/10.1016/j.commatsci.2010.05.010>
60. A.A. Bolzan, C. Fong, B.J. Kennedy, C.J. Howard, Structural studies of rutile-type metal dioxides. *Acta Crystallogr. Sect. B Struct. Sci.* 53(3), 373 (1997). <https://doi.org/10.1107/S0108768197001468>
61. D. McWhan, M. Marezio, J. Remeika, P. Dernier, X-ray diffraction study of metallic VO<sub>2</sub>. *Phys. Rev. B* 10(2), 490 (1974). <https://doi.org/10.1103/PhysRevB.10.490>
62. G.A. Seisenbaeva, M. Sundberg, M. Nygren, L. Dubrovinsky, V.G. Kessler, Thermal decomposition of the methoxide complexes MoO(OMe)<sub>4</sub>, Re<sub>4</sub>O<sub>6</sub>(OMe)<sub>12</sub> and (Re<sub>1-x</sub>Mo<sub>x</sub>)O<sub>6</sub>(OMe)<sub>12</sub> (0.24 ≤ x ≤ 0.55). *Match. Chem. Phys.* 87(1), 142 (2004). <https://doi.org/10.1016/j.matchemphys.2004.05.025>
63. G. Demazeau, A. Baranov, R. Poettgen, L. Kienle, M.H. Moeller, R.D. Hoffmann, M. Valldor, An anhydrous high-pressure synthesis route to rutile type RhO<sub>2</sub>. *Z. Naturforsch. B* 61(12), 1500 (2006). <https://doi.org/10.1515/znb-2006-1206>
64. A. Ivanovskii, T. Chupakhina, V. Zubkov, A. Tyutyunnik, V. Krasilnikov, G. Bazuev, S. Okatov, A. Lichtenstein, Structure and electronic properties of new rutile-like rhenium (IV) dioxide ReO<sub>2</sub>. *Phys. Lett. A* 348(1–2), 66 (2005). <https://doi.org/10.1016/j.physleta.2005.08.025>
65. C.E. Boman, Precision determination of the crystal structure of osmium dioxide. *Acta Chem. Scand.* 24(1), 123 (1970). <https://doi.org/10.3891/acta.chem.scand.24-0123>
66. M.H. Fernandez, B. Chamberland, A new high pressure form of PtO<sub>2</sub>. *J. Less Common Met.* 99(1), 99 (1984). [https://doi.org/10.1016/0022-5088\(84\)90338-2](https://doi.org/10.1016/0022-5088(84)90338-2)
67. P. D'Antonio, A. Santoro, Powder neutron diffraction study of chemically prepared β-lead dioxide. *Acta Crystallogr. Sect. B Struct. Crystallogr. Cryst. Chem.* 36(10), 2394 (1980). <https://doi.org/10.1107/S0567740880008813>
68. G. Bergerhoff, I. Brown, F. Allen et al., Crystallographic databases. *Int Union Crystallogr. Chester* 360, 77 (1987)
69. J. Riga, C. Tenret-Noël, J.J. Pireaux, R. Caudano, J.J. Verbist, Y. Gobillon, Electronic structure of rutile oxides TiO<sub>2</sub>, RuO<sub>2</sub> and IrO<sub>2</sub> studied by x-ray photoelectron spectroscopy. *Phys. Scr.* 16(5–6), 351 (1977). <https://doi.org/10.1088/0031-8949/16/5-6/027>
70. D. Payne, G. Paolicelli, F. Offi, G. Panaccione, P. Lacovig, G. Beamson, A. Fondacaro, G. Monaco, G. Vanko, R. Egdel, A study of core and valence levels in β-PbO<sub>2</sub> by hard x-ray photoemission. *J. Electron Spectros. Relat. Phenom.* 169(1), 26 (2009). <https://doi.org/10.1016/j.elspec.2008.10.002>
71. M. Stapelbroek, B. Evans, Exciton structure in the u.v.-absorption edge of tetragonal GeO<sub>2</sub>. *Solid State Commun.* 25(11), 959 (1978). [https://doi.org/10.1016/0038-1098\(78\)90311-3](https://doi.org/10.1016/0038-1098(78)90311-3)
72. F. Arlinghaus, Energy bands in stannic oxide (SnO<sub>2</sub>). *J. Phys. Chem. Solids* 35(8), 931 (1974). [https://doi.org/10.1016/S0022-3697\(74\)80102-2](https://doi.org/10.1016/S0022-3697(74)80102-2)
73. J.E. Post, Manganese oxide minerals: crystal structures and economic and environmental significance. *Proc. Natl. Ac. Sci.* 96(7), 3447 (1999). <https://doi.org/10.1073/pnas.96.7.3447>
74. J.B. Goodenough, Metallic oxides. *Prog. Solid State Chem.* 5, 145 (1971). [https://doi.org/10.1016/0079-6786\(71\)90018-5](https://doi.org/10.1016/0079-6786(71)90018-5)
75. H. Sato, T. Enoki, M. Isobe, Y. Ueda, Transport properties and magnetism of a helically hund-coupled conductor: β - MnO<sub>2</sub>. *Phys. Rev. B* 61, 3563 (2000). <https://doi.org/10.1103/PhysRevB.61.3563>
76. A.A. Bolzan, C. Fong, B.J. Kennedy, C.J. Howard, A powder neutron diffraction study of semiconducting and metallic niobium dioxide. *J. Solid State Chem.* 113(1), 9 (1994). <https://doi.org/10.1006/jssc.1994.1334>
77. K. Jacob, V. Saji, J. Gopalakrishnan, Y. Waseda, Thermodynamic evidence for phase transition in MoO<sub>2-δ</sub>. *J. Chem. Thermodyn.* 39(12), 1539 (2007). <https://doi.org/10.1016/j.jct.2007.09.005>
78. S. Shibata, Y. Hirose, A. Chikamatsu, E. Ikenaga, T. Hasegawa, Strain-induced structural transition of rutile type ReO<sub>2</sub> epitaxial thin films. *Appl. Phys. Lett.* 117(11), 111903 (2020). <https://doi.org/10.1063/5.0006373>
79. F. Tran, J. Stelzl, P. Blaha, Rungs 1 to 4 of DFT Jacobs ladder: extensive test on the lattice constant, bulk modulus, and cohesive energy of solids. *J. Chem. Phys.* 144, 204120 (2016). <https://doi.org/10.1063/1.4948636>
80. E. Ortel, T. Reier, P. Strasser, R. Kraehnert, Mesoporous IrO<sub>2</sub> films templated by peo-pb-peo block-copolymers: self-assembly, crystallization behavior, and electrocatalytic performance. *Chem. Mater.* 23(13), 3201 (2011). <https://doi.org/10.1021/cm200761f>
81. E. Ortel, J. Polte, D. Bernsmeier, B. Eckhardt, B. Paul, A. Bergmann, P. Strasser, F. Emmerling, R. Kraehnert, Pd/TiO<sub>2</sub> coatings with template-controlled mesopore structure as highly active

- hydrogenation catalyst. *Appl. Catal. A Gen.* 493, 25 (2015). <https://doi.org/10.1016/j.apcata.2014.12.044>
82. C.J. Brinker, Y. Lu, A. Sellinger, H. Fan, Evaporation-induced self-assembly: nanostructures made easy. *Adv. Mater.* 11(7), 579 (1999)
83. M. Landmann, E. Rauls, W. Schmidt, The electronic structure and optical response of rutile, anatase and brookite TiO<sub>2</sub>. *J. Phys. Cond. Mat.* (2012). <https://doi.org/10.1088/0953-8984/24/19/195503>
84. W. Yan, X. Liu, Niobium-doped TiO<sub>2</sub>: effect of an interstitial oxygen atom on the charge state of niobium. *Inorg. Chem.* 58(5), 3090 (2019). <https://doi.org/10.1021/acs.inorgchem.8b03096>
85. H.Y. Lee, S.J. Clark, J. Robertson, *MRS Online Proc. Librar.* 1352(1), 3 (2011). <https://doi.org/10.1557/opl.2011.1007>
86. H. Nakai, J. Heyd, G.E. Scuseria, Periodic-boundary-condition calculation using heyd-scuseria-ernzerhof screened coulomb hybrid functional: electronic structure of anatase and rutile TiO<sub>2</sub>. *J. Comput. Chem. Jpn.* 5(1), 7 (2006). <https://doi.org/10.2477/jccj.5.7>
87. A. Malashevich, M. Jain, S.G. Louie, First-principles dft+gw study of oxygen vacancies in rutile TiO<sub>2</sub>. *Phys. Rev. B* 89(7), 075205 (2014). <https://doi.org/10.1103/PhysRevB.89.075205>
88. A.C. Ulpe, K.C. Bauerfeind, T. Bredow, Influence of spin state and cation distribution on stability and electronic properties of ternary transition-metal oxides. *ACS Omega* 4(2), 4138 (2019). <https://doi.org/10.1021/acsomega.8b03254>
89. H.Y. Lee, J. Robertson, Doping and compensation in Nb-doped anatase and rutile TiO<sub>2</sub>. *J. Appl. Phys.* 113(21), 213706 (2013). <https://doi.org/10.1063/1.4808475>
90. T. Yamamoto, T. Ohno, Screened hybrid density functional study on Nb- and Ta-doped TiO<sub>2</sub>. *Phys. Rev. B* 85(3), 033104 (2012). <https://doi.org/10.1103/PhysRevB.85.033104>
91. Y. Tezuka, S. Shin, T. Ishii, T. Ejima, S. Suzuki, S. Sato, Photoemission and bremsstrahlung isochromat spectroscopy studies of TiO<sub>2</sub> (rutile) and SrTiO<sub>3</sub>. *J. Phys. Soc. Jpn.* 63(1), 347 (1994). <https://doi.org/10.1143/jpsj.63.347>
92. S. Rangan, S. Katalinic, R. Thorpe, R.A. Bartynski, J. Rochford, E. Galoppini, Energy level alignment of a zinc (ii) tetraphenylporphyrin dye adsorbed onto TiO<sub>2</sub> (110) and ZnO (1120) surfaces. *J. Phys. Chem. C* 114(2), 1139 (2010). <https://doi.org/10.1021/jp909320f>
93. K. Yang, Y. Dai, B. Huang, Y.P. Feng, First-principles gga+u study of the different conducting properties in pentavalent-ion-doped anatase and rutile TiO<sub>2</sub>. *J. Phys. D Appl. Phys.* 47(27), 275101 (2014). <https://doi.org/10.1088/0022-3727/47/27/275101>
94. B.J. Morgan, D.O. Scanlon, G.W. Watson, Small polarons in Nb- and Ta-doped rutile and anatase TiO<sub>2</sub>. *J. Mater. Chem.* 19(29), 5175 (2009). <https://doi.org/10.1039/B905028K>

**Publisher's Note** Springer Nature remains neutral with regard to jurisdictional claims in published maps and institutional affiliations.